



Fully controllable time-bin entangled states distributed over 100-km single-mode fibers

Jinwoo Kim¹, Jiho Park^{1*}, Hong-Seok Kim¹, Guhwan Kim¹, Jin Tae Kim¹, Jaegy Park¹, Kiwon Moon¹, Seung-Chan Kwak², Min-su Kim¹ and Jung Jin Ju¹

*Correspondence:
jiho5329@etri.re.kr

¹Quantum Sensing Research
Section, Electronics and
Telecommunications Research
Institute, Daejeon, 34129, Republic
of Korea

Full list of author information is
available at the end of the article

Abstract

Quantum networks that can perform user-defined protocols beyond quantum key distribution will require fully controllable entangled quantum states. To expand the available space of generated time-bin entangled states, we demonstrate a time-bin entangled photon source that produces qubit states $|\psi\rangle = \alpha|00\rangle + \beta|11\rangle$ with fully controllable phase and amplitudes. Eight different two-photon states have been selected and prepared from arbitrary states on the reduced two-qubit Bloch sphere. The photon pairs encoded in the time-bin scheme were generated at 2.4 MHz with a visibility of $V = 0.9475 \pm 0.0016$, with a violation of the CHSH Bell's inequality by 197 standard deviations. After entanglement distribution over 100 km of single-mode fibers, we obtained a visibility of $V = 0.9541 \pm 0.0113$ with a violation of the CHSH Bell's inequality by 6 standard deviations. The prepared states had an average fidelity of 0.9540 ± 0.0016 at the source and an average fidelity of $0.9353^{+0.0100}_{-0.0209}$ after entanglement distribution, which shows that the quantum states generated by our time-bin entangled photon source can be fully controlled potentially to a level applicable to long-distance advanced quantum network systems.

Keywords: Quantum communication; Quantum networks; Entanglement distribution; Time-bin qubits

1 Introduction

Entanglement is an essential resource in the realization of quantum networks [1, 2]. The protocols for long-distance quantum communication [3–6], like quantum teleportation [7–11] and entanglement swapping [12–14] rely on distributed entanglement. Currently, the most popular forms of qubit encodings for entanglement sources are polarization [15–17] and time-bin encodings [18–20]. Time-bin encoding can be more robust in long-distance transmission through optical fibers [21–23] because time-bin encoding inherently exhibits resistance to uncontrollable polarization fluctuations [24, 25] and polarization mode dispersion [23] in deployed fibers, factors that could induce decoherence in polarization qubit states [26]. However, implementing unitary operations and measurements in arbitrary bases is non-trivial for time-bin qubits compared to polarization qubits. Previous studies have explored arbitrary entangled polarization qubits [27], time-bin to polar-

© The Author(s) 2024. **Open Access** This article is licensed under a Creative Commons Attribution-NonCommercial-NoDerivatives 4.0 International License, which permits any non-commercial use, sharing, distribution and reproduction in any medium or format, as long as you give appropriate credit to the original author(s) and the source, provide a link to the Creative Commons licence, and indicate if you modified the licensed material. You do not have permission under this licence to share adapted material derived from this article or parts of it. The images or other third party material in this article are included in the article's Creative Commons licence, unless indicated otherwise in a credit line to the material. If material is not included in the article's Creative Commons licence and your intended use is not permitted by statutory regulation or exceeds the permitted use, you will need to obtain permission directly from the copyright holder. To view a copy of this licence, visit <http://creativecommons.org/licenses/by-nc-nd/4.0/>.

ization qubits conversions for arbitrary measurement [28, 29], or control of single time-bin qubits [30], but not the manipulation or control of two entangled time-bin qubits.

Ultimately, users of quantum networks may desire the creation of states beyond a single Bell state, e.g. $|\Phi^+\rangle$, generated by typical entangled photon source systems for the facilitation of user-defined experiments [31, 32]. For example, with control over phase, protocols such as three-partite quantum secret sharing can be enabled [33]. With additional control over probability amplitudes, partially entangled states can be created for partial teleportation [34] potentially for further optimization of teleportation [35]. The full control over generating entangled states may therefore become an important feature of quantum networks.

However, the state-controlled distribution of entangled time-bin qubits has not been experimentally demonstrated. In typical time-bin entangled qubit generation, two-qubit states were prepared by unbalanced Mach-Zehnder interferometers (UMZIs) [21, 36] or by electro-optic intensity modulators [10, 14, 37] with no control over probability amplitudes.

In this work, we aim to provide a more user-programmable quantum network by expanding the coverage of time-bin entangled states on the two-qubit Bloch sphere. Specifically, we prepare two-qubit time-bin states $|\psi\rangle = \alpha|00\rangle + \beta|11\rangle$ with fully controllable phase and amplitudes. We generate these entangled photon pairs via spontaneous parametric down-conversion (SPDC) at high count rates and fidelity. We evaluate the quality of entanglement by observing two-photon interference in generated Bell pairs with high visibility and a significant degree of violation of the Clauser-Horne-Shimony-Holt (CHSH) inequality [38].

We further demonstrate that the quality of entanglement is maintained even after distributing entangled photons over 100-km of optical fibers. While other groups typically used dispersion shifted fibers (DSFs) to distribute entangled photon pairs [10, 22, 23, 39], we distributed our time-bin two-qubit states using two 50-km standard single-mode fiber (SMF) fiber spools. We compensated for the chromatic dispersion of SMF with dispersion compensating fibers (DCFs). Through quantum state tomography, we show that the fidelities of our prepared states remain consistent before and after distribution, demonstrating a system qualified and stable enough for higher complexity quantum communication protocols.

2 State controlled time-bin entanglement generation

A typical process for time-bin entanglement generation via SPDC is as follows. Temporally separated double pump pulses are created with a pulsed laser or a CW laser modulated by an intensity modulator. In our setup, the pump wavelength is in the telecom C-band, and the modulated pulses are frequency-doubled via second harmonic generation (SHG) and then converted back into the telecom C-band as entangled photon pairs through SPDC [9, 10, 37, 40]. After SPDC, signal and idler photons are produced at the single photon level with a low mean photon number ($\mu \ll 1$). The resulting states of the photons are described by [39]

$$\alpha|0\rangle_s|0\rangle_i + \beta|1\rangle_s|1\rangle_i, \quad (1)$$

where $|0\rangle$ ($|1\rangle$) is the early (late) temporal mode, α and β are time-bin state amplitudes with $|\alpha|^2 + |\beta|^2 = 1$, and subscripts s and i indicate signal and idler respectively.

The control and preparation of time-bin states can be done classically before SPDC using an intensity modulator and a phase modulator. The intensity modulator controls $|\alpha\rangle$ and $|\beta\rangle$ by modulating the intensity of the double pump peaks to different initial levels, and the phase modulator controls the phase difference between α and β by acting on only one pulse.

Experimentally, the temporal states $|0\rangle$ and $|1\rangle$ have specific pulse widths and a time delay between the two time-bin pulses. A requirement for choosing these time-bin pulse parameters is that the generated states $|0\rangle$ and $|1\rangle$ must be orthogonal.

The temporal states $|0\rangle$ and $|1\rangle$ can be represented by Gaussian time-bin pulses [41]:

$$|0\rangle = \int_{-\infty}^{\infty} dt \frac{1}{(\pi\sigma^2)^{1/4}} \exp\left[-\frac{(t + \tau/2)^2}{2\sigma^2}\right] |t\rangle, \quad (2)$$

$$|1\rangle = \int_{-\infty}^{\infty} dt \frac{1}{(\pi\sigma^2)^{1/4}} \exp\left[-\frac{(t - \tau/2)^2}{2\sigma^2}\right] |t\rangle, \quad (3)$$

where τ is the time delay between time-bin pulses, and σ is the standard deviation of the time-bin pulse width. From this definition we can derive that the orthogonality between states $|0\rangle$ and $|1\rangle$ depends on the ratio of τ to σ [41]:

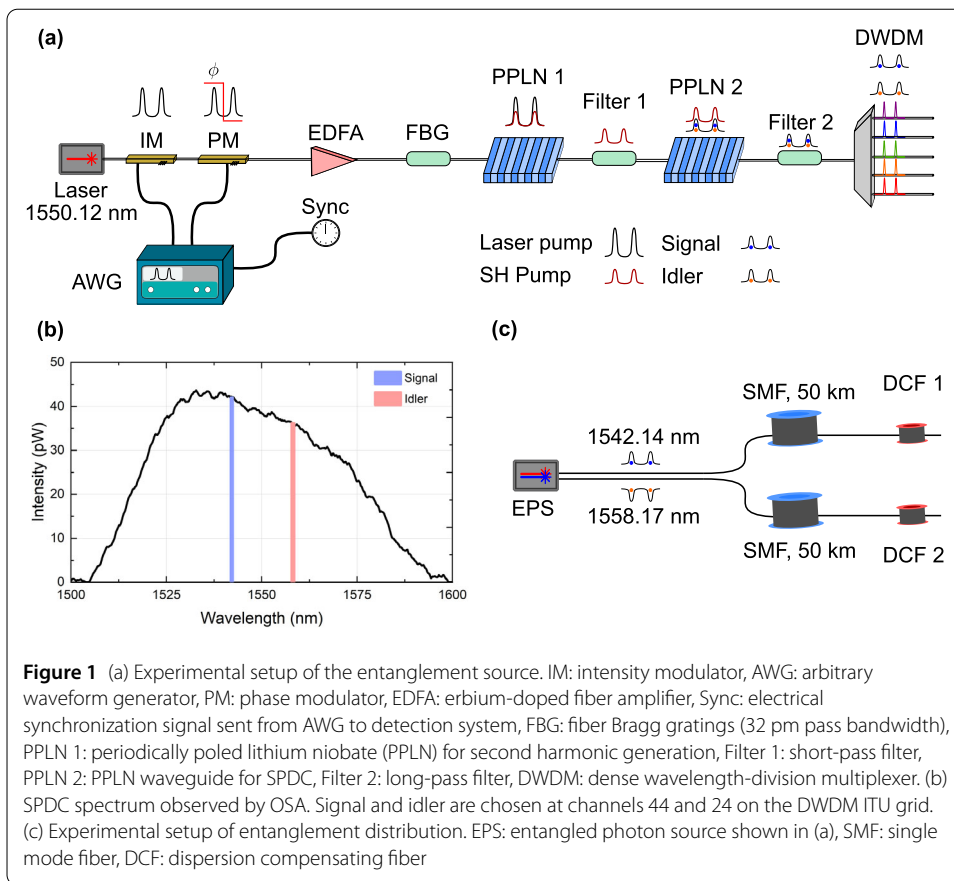
$$\langle 0|1\rangle = \exp\left(\frac{-\tau^2}{4\sigma^2}\right). \quad (4)$$

Lower τ are desired to maximize the generation of quantum states. However, dispersion applies a unitary operation that widens σ upon transmission through optical fiber. This may lead to higher $\langle 0|1\rangle$ upon measurement, resulting in higher error rates due to overlap in temporal modes [20]. To compensate for dispersion and to reduce error rates, linear optics can be employed before or after distribution through optical fiber [15, 18, 19, 42].

3 Experimental scheme

Our entanglement generation and distribution setup is shown in Fig. 1. We use a CW laser pump centered to channel 34 (1550.12 nm) on the dense wavelength-division multiplexing International Telecommunication Union (ITU) grid. We carve two pulses ($\sigma = 42.5$ ps, $\tau = 500$ ps) with a repetition rate of 200 MHz with an arbitrary waveform generator (AWG) and a lithium niobate intensity modulator. Both intensity and phase modulators (Thorlabs) act on the pump before SHG, monitored by an oscilloscope prior to SPDC. Our chosen values of τ and σ results in a pulse overlap $\langle 0|1\rangle$ of $\sim 10^{-15}$, minimizing errors due to non-orthogonal bases.

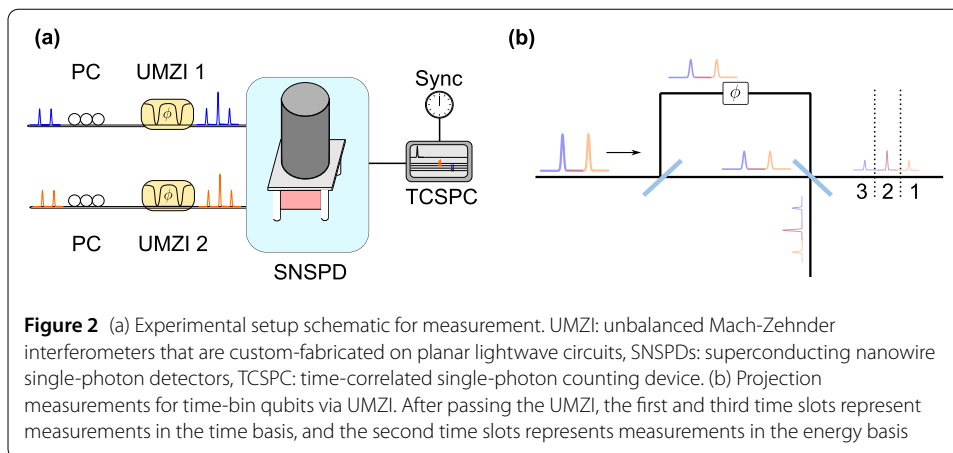
The pulses are amplified by an erbium-doped fiber amplifier (EDFA), and the noise spectrum generated from the EDFA is filtered by a fiber Bragg grating filter (EXFO XTM-50) with a 32-pm bandwidth. The filtered pulses undergo frequency-doubling by SHG on a type-0 periodically poled lithium niobate (PPLN) waveguide (HCP WG Mixer) with a length of 10-mm and a normalized conversion efficiency of $\sim 80\%/W/\text{cm}^2$. SPDC generates signal and idler photons by using another type-0 PPLN waveguide (Covesion, WGP-M-1550-40) with a 40-mm length and an 18.5- μm poling period. The fundamental 1550 nm and second-harmonic (SH) 775 nm pumps are filtered out by short-pass (filter 1) and long-pass (filter 2) filters, respectively. A dense wavelength-division multiplexer (DWDM, General Photonics) with 200 GHz spacings separates the generated signal and idler photons based on the ITU grid.



The SPDC spectrum was observed via an optical spectrum analyzer as depicted in Fig. 1 (b). Operating at 54.5°C for our SPDC process resulted in a spectral FWHM of ~70 nm. This wide bandwidth is fully able to accommodate the simultaneous distribution of entangled photon pairs across the C-band and supports more complex wavelength division multiplexing schemes [43, 44]. In our experiments, we confirmed entanglement generation across ITU channels 20 through 48, covering wavelengths 1538 nm through 1562 nm. In this work, we select signal and idler photons on the ITU channels 44 (1542.14 nm) and 24 (1558.17 nm) to prepare and separate entangled photon pairs.

Each channel utilizes 50-km SMF spools for entanglement distribution. After distribution, DCF spools are employed for channels 24 and 44 with negative dispersion values of -1080 ps nm^{-1} was applied for DCF 1 and -720 ps nm^{-1} , respectively. While the dispersion values differ for each arm, the main importance of dispersion compensation is to regain the ability to distinguish time-bins after entanglement distribution. Once past the threshold for full distinguishability between time slots, any further negative dispersion neither hinders nor improves the quality of qubits as long as the coincidence window can encapsulate and distinguish photons measured in each time-bin. As we show later, both DCFs reduced the non-orthogonality of measurement in time-bin bases due to dispersion such that high visibility was recovered.

Characterization of time-bin entangled qubits requires a precise knowledge of fiber lengths. Measurement of SMFs and DCFs lengths involved comparing the cross-correlation peak times in a setup with and without fiber spools. As the cross-correlation peak



time indicates the moment when the signal and idler photons are simultaneously generated, a difference in path length of the signal or idler is reflected as a change in timing of the cross-correlation peak center by the extra time taken for the signal or idler to be transmitted through path length difference.

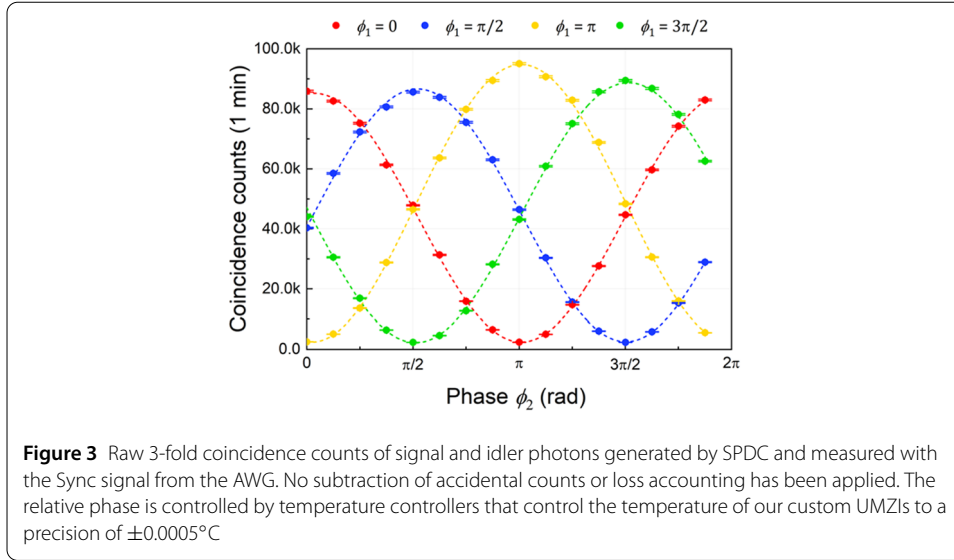
The measurement setup for time-bin encoded photons is shown in Fig. 2. Signal and idler photons are inserted into UMZI planar lightwave circuits (PLCs). The PLCs are fabricated such that the long arm has a time delay of $\tau = 500$ ps relative to the short arm. The time-bin states are characterized by post-selection after passing through a UMZI. The UMZIs divide the photons into three distinct time slots. The first and third time slots correspond to early and late qubits, respectively, where the early (late) pulse passes through the short (long) arm of the UMZI and is therefore temporally distinguishable. This is a measurement in the time basis. The second time slot is a projection measurement in the energy basis $(|0\rangle + e^{i\phi}|1\rangle)/\sqrt{2}$, observed when an early (late) pulse passes through the long (short) arm of the UMZI and becomes temporally indistinguishable [45].

Each UMZIs features a total insertion loss of 4.6 dB and 4.7 dB, which includes a 3 dB loss from the 50:50 split. For balanced optical power splitting, transmission loss is specifically engineered into the short arm to compensate for additional loss on the long arm. This adjustment resulted in an intensity ratio of 93.1 % and 93.7% for the early pulse to late pulse in UMZI 1 and UMZI 2, respectively. Phase differences between both arms are controlled by a temperature controller (Meerstetter Engineering TEC-1091) with $\pm 0.01^\circ\text{C}$ precision and stability of $\pm 0.0005^\circ\text{C}$. The full period of 2π was approximately 2°C for each UMZI. Each UMZI output port is connected to superconducting nanowire single-photon detectors (SNSPDs, Single Quantum) with detector efficiencies of 0.80 and 0.84, ~ 400 Hz dark count, ~ 30 ps jitter at FWHM, and ~ 20 ns dead time. Photon counts from the SNSPDs are analyzed using a time-correlated single-photon counter (TCSPC, HydraHarp 400), and the coincidence counts are recorded within a 200 ps coincidence time window.

4 Results

4.1 Entanglement characterization

Before distributing entanglement, we conducted measurements of two-photon interference fringes to characterize the degree of entanglement of time-bin entangled photons generated by SPDC. At an incident SH pump power of $89 \mu\text{W}$, we observed a coincidence count rate of 11.3 kHz at a coincidence-to-accidental count ratio (CAR) 309. This corre-



sponds to a pair generation rate of $R = 2.4$ MHz and an average photon number per qubit $\mu = 0.012$. The total detection efficiency for both signal and idler respectively, including the SNSPD detector efficiencies, SPDC output coupling loss, DWDM insertion loss, and other fiber losses, was $\eta_s (\eta_i) \simeq 0.0670$ (-11.74 dB loss) respectively (see Appendix A for details). To measure each interference fringe in Fig. 3, the phase of UMZI1 was held at a constant temperature, while the phase of UMZI2 was adjusted in steps of $\pi/8$ by changing the temperature incrementally at 0.125°C per measurement. We note that there is a drop in detected coincidence counts to a maximum of ~ 1500 Hz as shown on Fig. 3 due to an inherent loss in post-selection for measuring in the energy-basis [23] as well as the added insertion loss from the UMZI chips. Each data point was acquired for 1 minute, and the visibility of the fitted curves was $V = 0.9475 \pm 0.0016$ without subtracting accidental coincidences, exceeding the value of 0.7071 needed to confirm entanglement [38]. The visibility deviates from unity due to both multiple photon-pair generation and fabrication imperfections in the UMZIs [46, 47]. Theoretically, we expect that our visibility should give values according to [23, 48]:

$$V = \frac{\mu' \eta_s \eta_i / 4}{\mu' \eta_s \eta_i / 4 + 2(\mu' \eta_s / 2 + d_s)(\mu' \eta_i / 2 + d_i)}. \quad (5)$$

In this equation, $\mu' = \mu/2$ is the average number of photons per pulse. For our values $\mu = 0.012$, $\eta_s (\eta_i) \simeq 0.0464$ (0.0453) including extra loss from fabricated UMZIs, and dark counts per pulse $d_s = d_i \simeq 2 \times 10^{-6}$, we calculate that the theoretical visibility should be $V = 0.988$. The deviation in theoretical and experimental visibility arose due to a difference in optical loss between the short and long arm of our UMZI PLC chips.

The degree of Bell's inequality violation S can be measured via the CHSH inequality given by [38, 49]. From the two-photon interference fringes in Fig. 3, we extracted a CHSH violation of $S = 2.684 \pm 0.003$, a value above the classical threshold $S = 2$ by 197 standard deviations. This value indicates an extremely high degree of entanglement and confidence that our entangled photons exhibit a significantly quantum nature.

4.2 State control

Figure 4 demonstrates full controllability of entangled two-qubit states. States A through D were generated as $(|0\rangle_s|0\rangle_i + e^{i\phi}|1\rangle_s|1\rangle_i)/\sqrt{2}$ with $\phi = -\pi/2, 0, \pi/2, \pi$, respectively. This control was achieved by applying voltages $V_{-\pi/2} = 3.3$ V, $V_0 = 4.5$ V, $V_{\pi/2} = 5.7$ V, $V_\pi = 6.9$ V to the phase modulator, respectively. Similarly, the probability amplitude of the two-qubit time-bin states was controlled for states E through H by adjusting the voltage applied to the intensity modulator. The pulse amplitudes were monitored by measuring the SH pump's early and late pulse powers using the SH pump's early and late pulse powers used for states A through D as reference points.

To measure and confirm the control of quantum bits, quantum state tomography was conducted as outlined in [50, 51] and as shown explicitly for time-bin states in [37]. Our UMZIs were set in 4 combinations of temperatures of $T_1, T_2 = (26.070^\circ\text{C}, 29.130^\circ\text{C})$, $(26.070^\circ\text{C}, 29.630^\circ\text{C})$, $(26.570^\circ\text{C}, 29.130^\circ\text{C})$, $(26.570^\circ\text{C}, 29.630^\circ\text{C})$, which correspond to projection measurements in $|++\rangle, |+L\rangle, |L+\rangle, |LL\rangle$ states respectively, with states $|+\rangle, |L\rangle$ corresponding to $|+\rangle = (|0\rangle + |1\rangle)/\sqrt{2}$ and $|L\rangle = (|0\rangle + i|1\rangle)/\sqrt{2}$. Overall, the set of states $\{|0\rangle, |1\rangle, |+\rangle, |L\rangle\}$ was used to uniquely determine a density matrix ρ . The density matrix obtained in this manner was further optimized using maximum likelihood estimation (MLE) [52] by maximizing $P(\mathcal{M}|\rho)$, the probability that a dataset \mathcal{M} would have been measured

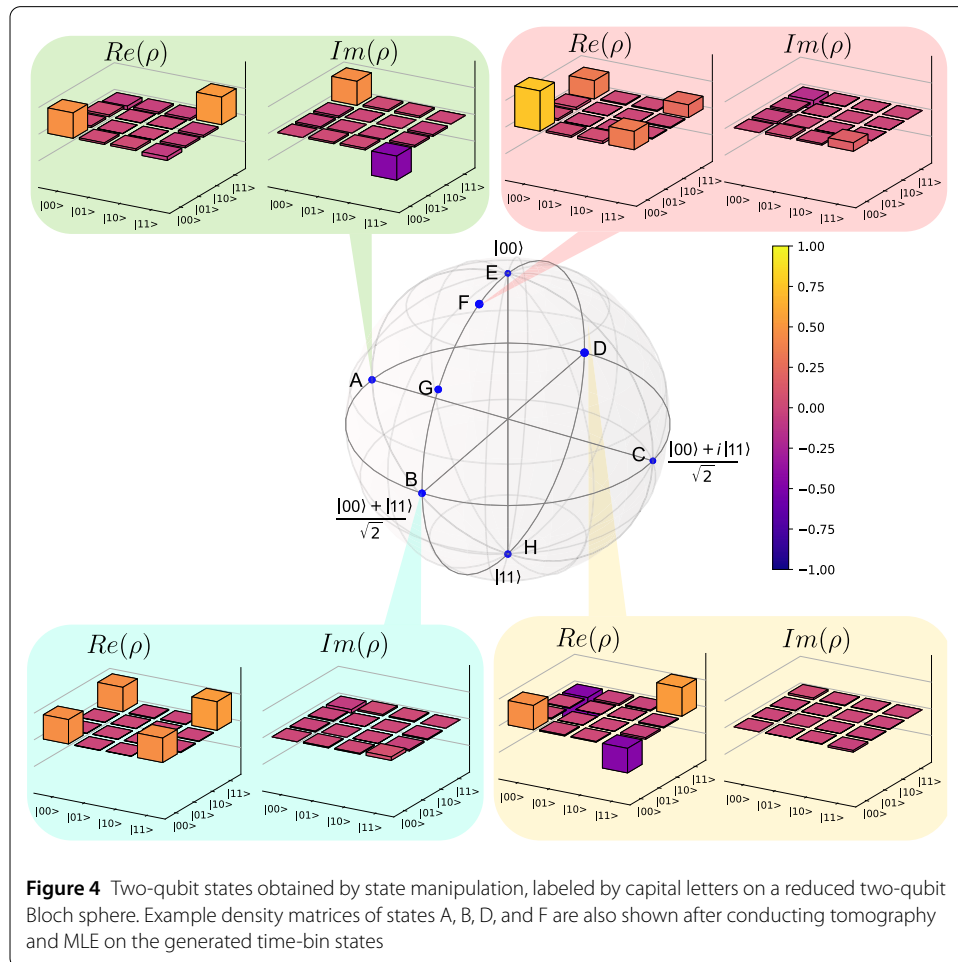
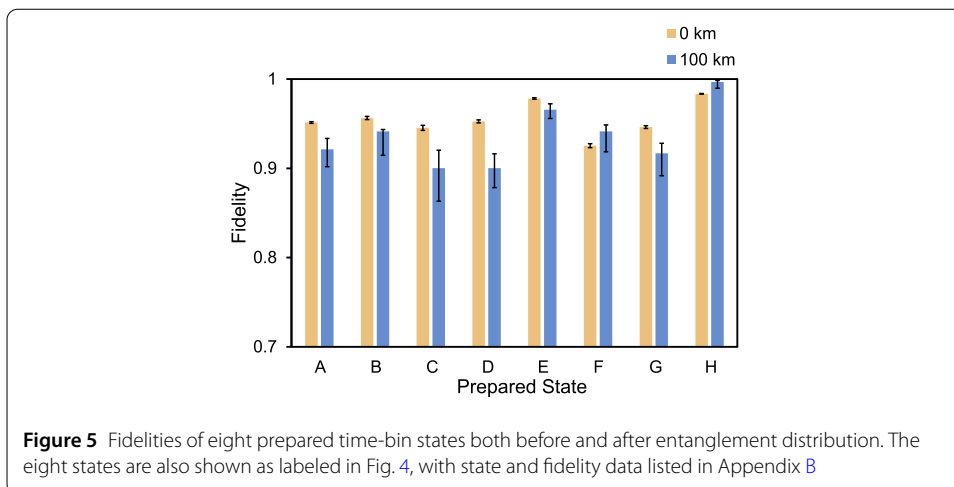


Figure 4 Two-qubit states obtained by state manipulation, labeled by capital letters on a reduced two-qubit Bloch sphere. Example density matrices of states A, B, D, and F are also shown after conducting tomography and MLE on the generated time-bin states



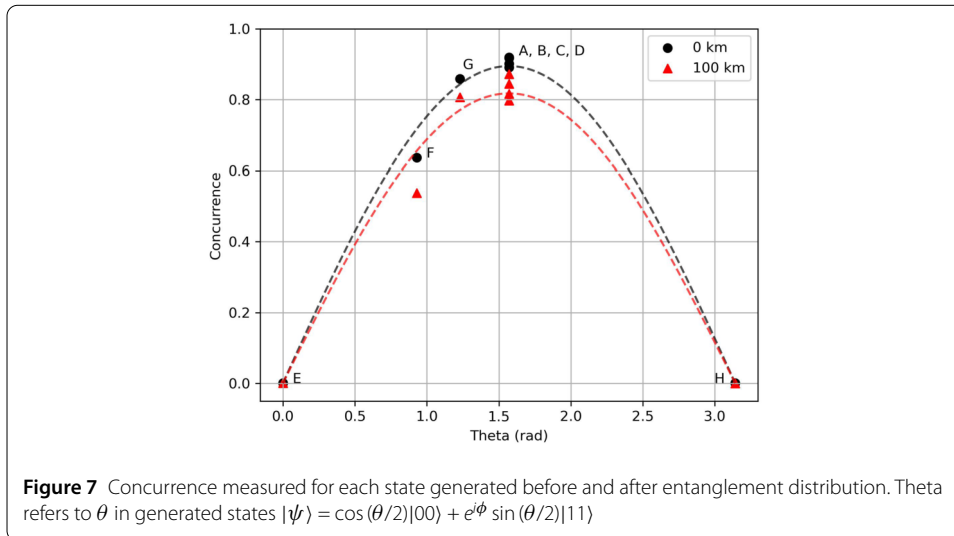
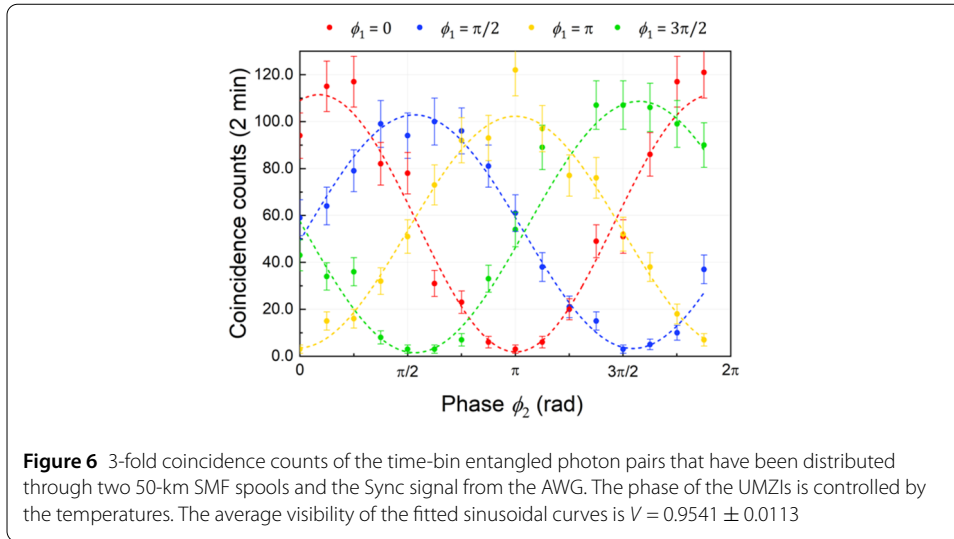
given that the quantum state was set as ρ before measurement. MLE was implemented as described in [51] to obtain a final density matrix.

The fidelities of all the measured states are shown in Fig. 5. The average fidelity measured at the source for all eight states was 0.9540 ± 0.0016 . See Appendix B for further details on fidelity data and error calculations. When measuring our time-bin qubits, counts for state $|00\rangle$ was 12.7% lower than $|11\rangle$, which is reflected in the calculated density matrices. This is due to a difference in optical transmission ratio of $|0\rangle$ and $|1\rangle$ while passing through UMZIs, with each UMZI exhibiting 93.1% and 93.7% transmission loss ratio of $|0\rangle$ to $|1\rangle$ respectively. The effect of different transmission loss ratios was also reflected in the state fidelity, resulting in deviations from unity. We note that the states $|00\rangle$ (E) and $|11\rangle$ (H) are inherently less affected because no interference is needed for measurement. This results in higher fidelity for states $|00\rangle$ and $|11\rangle$ than other states.

4.3 Entanglement distribution

We distributed the entangled photon pairs across two 50-km SMF spools and observed two-photon interference patterns after dispersion compensation using DCFs. All other measurement settings remained unchanged before entanglement distribution. Figure 6 displays the 3-fold coincidence counts of the distributed entangled photon pairs, with each data point representing a measurement acquired for 2 minutes. The three-fold coincidence rate decreased from approximately 1500 Hz to ~ 1 Hz post-distribution due to losses in the SMFs (0.22 dB/km) and DCFs (3.0 dB for DCF 1, 4.5 dB for DCF 2).

Without DCFs, the visibility dropped significantly below the quantum boundary of 0.7071 due to chromatic dispersion in the SMFs. Each time-bin pulse expanded to $\sigma = 382.2$ ps. The increased pulse width resulted in $\langle 0|1\rangle = 0.651$, indicating a high non-orthogonality between time-bin states. With DCFs reducing dispersion, pulses were restored to $\sigma = 93.4$ ps and $\sigma = 72.2$ ps for signal and idler channels, respectively. This led to a reduction in non-orthogonality to $\langle 0|1\rangle \sim 10^{-3}$ and 10^{-5} for signal and idler channels, respectively. The reduction in non-orthogonality also restored the visibility of the interference fringes to $V = 0.9541 \pm 0.0113$. The visibility of the fringes mainly depends on the SH pump power (via the probability of multiple photon-pair emission in SPDC), the inherent interference quality of the UMZIs, detector noise, and dispersion [42]. As the pump power was maintained such that $\mu = 0.012$, consistent visibility was observed be-



fore and after entanglement distribution once dispersion was accounted for, as expected. CHSH calculations yielded $S = 2.667 \pm 0.109$, showing that a high degree of entanglement is maintained even after entanglement distribution, with a violation of the CHSH Bell’s inequality by 6 standard deviations.

The eight different two-qubit states depicted in Fig. 4 with different θ and ϕ on the Bloch sphere have also been transmitted through the two 50-km SMF spools. Fidelity comparisons are shown in Fig. 5. The average fidelity measured after entanglement distribution for all 8 generated states was $0.9353^{+0.0100}_{-0.0209}$.

When the measured count rate is low, error calculations show that the fidelity can have asymmetrical errors (see Appendix B). This is particularly true for the case after entanglement distribution, as shown in Fig. 5. Therefore, for states such as F or H, the fidelity derived from measured counts may be higher after entanglement distribution. However, Monte-Carlo simulations show that the average simulated fidelity is actually lower after entanglement distribution as expected (see Appendix B).

Furthermore, fidelity may not always be the most accurate method of measuring the degree of decoherence upon transmission. Another way to measure the degree of entanglement is by measuring the concurrence [51]. The concurrence was measured for each state and is shown in Fig. 7.

Concurrence measurements show that the degree of entanglement is controllable in generated states $|\psi\rangle = \alpha|00\rangle + \beta|11\rangle$. Concurrence is minimal for completely separable states $|00\rangle$ and $|11\rangle$, and the concurrence is maximal for Bell states as expected. Upon transmission through fiber channels, the decrease in concurrence shows a degradation in the degree of entanglement for all states.

5 Conclusions

We have experimentally demonstrated full controllability in both phase and amplitude of two-photon time-bin entangled qubits with an average fidelity of 0.9540 ± 0.0016 at the source and $0.9353^{+0.0100}_{-0.0209}$ after 100-km distribution over SMFs. Our system generates controllable entangled time-bin quantum states with a pair generation rate of 2.4 MHz. We successfully distributed eight different two-qubit states over 100-km SMFs while maintaining high visibility and state fidelity. Using this system, we detected 11.3 kHz coincidence counts with a CAR value of 309. We obtained a high degree of entanglement with $S = 2.684 \pm 0.003$ before entanglement distribution and $S = 2.667 \pm 0.109$ after entanglement distribution. To further increase coincidence count rates, the repetition rate can easily be increased by fully utilizing the high sampling rates of commercially available AWGs to improve the generation rate of entangled photon pairs vastly. Additional improvements can be made to the DWDM to not only decrease optical loss but to also fully exploit the 70 nm bandwidth of the SPDC source for multi-partite communication protocols. Overall, we provide an important tool to improve the flexibility of available quantum communication protocols by increasing controllability over entangled time-bin qubit states at high count rates and fidelities. The increased degree of freedom makes our system an ideal candidate for laying the foundation to create reconfigurable quantum networks in the future.

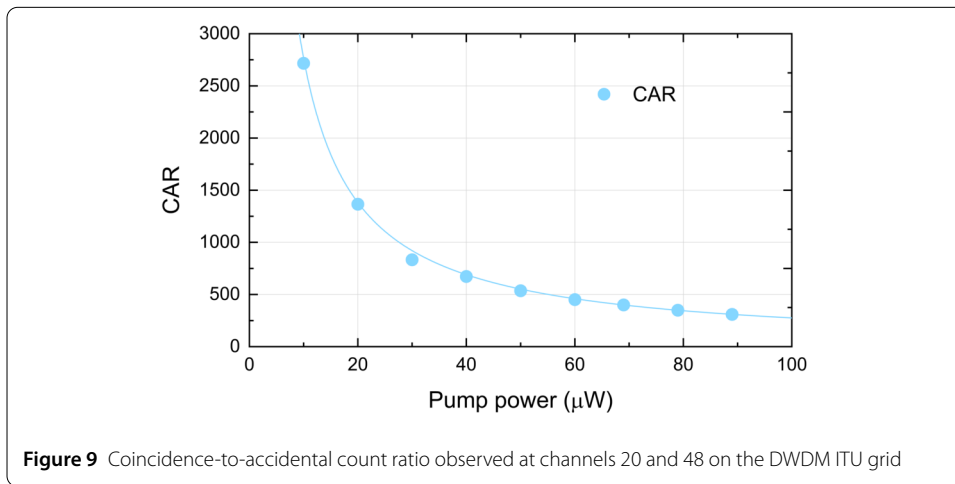
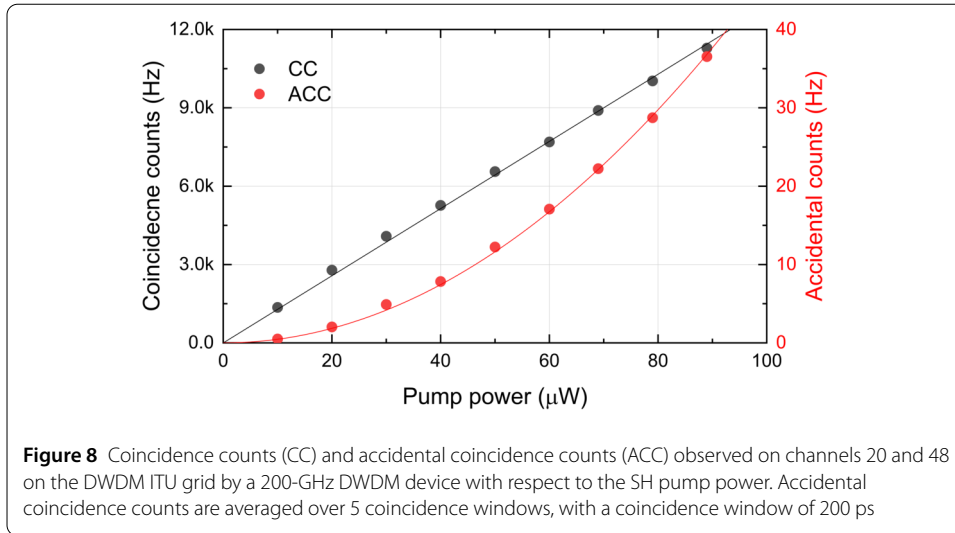
Appendix A: Source characterization details

In Fig. 8, we show the measured coincidence count rate and accidental coincidence count rate in relation to SH pump power, the average power measured with a power meter before the SPDC PPLN. The coincidence to accidental count ratio (CAR) in relation to the SH pump power is also shown in Fig. 9. In this work, we chose our SH pump power to be $89 \mu\text{W}$, as this gave a high coincidence count rate of 11.3 kHz as well as a reasonable CAR, which is defined as

$$CAR = \frac{N_{CC} - N_{ACC}}{N_{ACC}}, \quad (6)$$

where N_{CC} is the coincidence counts within the coincidence window, and N_{ACC} is the accidental coincidence counts. We characterized N_{ACC} as the average counts in coincidence windows within 5 repetition pulses away from the main coincidence counts window. At a SH pump power of $89 \mu\text{W}$, CAR had a value of 309. We used the following relations [53]

$$N_s = R\eta_s + D_s N_i = R\eta_i + D_i N_{CC} = R\eta_s \eta_i + N_{ACC}, \quad (7)$$



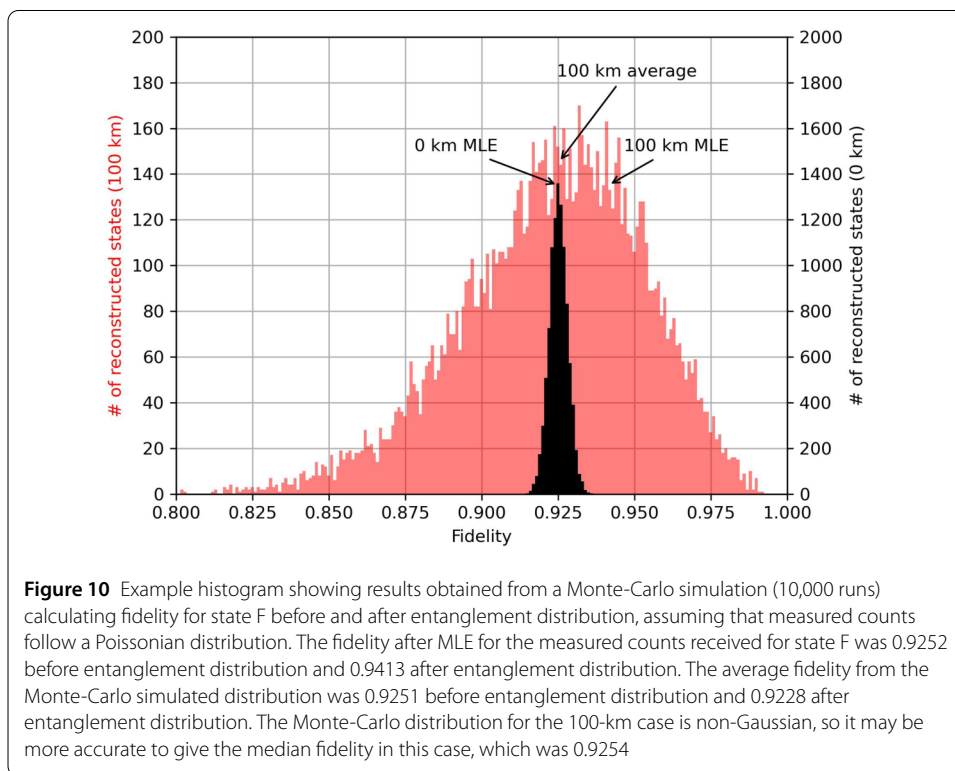
where N_s , N_i , N_{CC} , and N_{ACC} are the measured signal counts, idler counts, coincidence counts, and accidental coincidence counts respectively, D_s and D_i are dark counts measured for signal and idler channels, R is the generation rate of photon pairs and η_s and η_i are the detection efficiencies of signal and idler photons accounting for the total loss in each detection arm after SPDC. From these relations, we found R to calculate our mean photon number $\mu = R/R_{Rep}$, where R_{Rep} is our pump repetition rate of 200 MHz. For our SH pump power of 89 μW , we obtained a pair generation rate of 2.4 MHz with an average photon number $\mu = 0.012$.

Appendix B: Additional notes on fidelity

Table 1 shows all fidelities of prepared states before and after entanglement distribution. The errors for the fidelities were obtained by conducting a Monte-Carlo simulation assuming that the measured counts follow a Poissonian-like distribution. For each set of simulated counts, quantum state tomography and MLE is conducted to obtain a distribution of fidelities. An example simulation is shown in Fig. 10 with 10,000 runs for state F to find the distribution of fidelities assuming a Poissonian distribution of counts. The

Table 1 Fidelities of prepared time-bin states $|\psi\rangle = \cos(\theta/2)|00\rangle + e^{i\phi} \sin(\theta/2)|11\rangle$ both before and after entanglement distribution

State	(θ, ϕ)	\mathcal{F} (0 km)	\mathcal{F} (100 km)
A	$(\pi/2, 3\pi/2)$	0.9456 ± 0.0017	$0.9211^{+0.0122}_{-0.0195}$
B	$(\pi/2, 0)$	0.9562 ± 0.0018	$0.9413^{+0.0002}_{-0.0269}$
C	$(\pi/2, \pi/2)$	0.9452 ± 0.0028	$0.9000^{+0.0202}_{-0.0370}$
D	$(\pi/2, \pi)$	0.9524 ± 0.0017	$0.9000^{+0.0161}_{-0.0218}$
E	$(0, 0)$	0.9780 ± 0.0008	$0.9655^{+0.0066}_{-0.0098}$
F	$(0.93, 0)$	0.9252 ± 0.0022	$0.9413^{+0.0071}_{-0.0230}$
G	$(1.23, 0)$	0.9460 ± 0.0015	$0.9167^{+0.0113}_{-0.0252}$
H	$(\pi, 0)$	0.9833 ± 0.0004	$0.9914^{+0.0018}_{-0.0070}$



errors are given to reflect the distribution of fidelities. After entanglement distribution, the measured counts are lower. This means that the Poissonian error distribution is wider, thus resulting in a wider fidelity distribution.

Figure 10 also shows that the fidelity of the state is not actually improved upon distribution through the fiber channel for states such as state F. While the fidelity calculated post MLE for state F after entanglement distribution gives 0.9413, the average fidelity from the Monte-Carlo simulated distribution is 0.9254. On the other hand, in the 0-km case, the fidelity calculated from the density matrix post MLE corresponds to the average fidelity from the Monte-Carlo simulation. This is also shown in Table 1, thus showing that the average fidelity after Monte-Carlo simulations reflects a lower fidelity after entanglement distribution for all states. The asymmetrical errors are given to reflect these mismatches between the fidelity derived from measured counts and the Monte-Carlo distribution.

Table 2 Concurrences of prepared time-bin states $|\psi\rangle = \cos(\theta/2)|00\rangle + e^{i\phi} \sin(\theta/2)|11\rangle$ both before and after entanglement distribution

State	(θ, ϕ)	C (0 km)	C (100 km)
A	$(\pi/2, 3\pi/2)$	0.9194 ± 0.0041	$0.8442^{+0.0655}_{-0.0819}$
B	$(\pi/2, 0)$	0.9173 ± 0.0056	$0.8722^{+0.1263}_{-0.1743}$
C	$(\pi/2, \pi/2)$	0.9015 ± 0.0059	$0.8164^{+0.0769}_{-0.1019}$
D	$(\pi/2, \pi)$	0.8910 ± 0.0094	$0.7970^{+0.1258}_{-0.1754}$
E	(0, 0)	0.0008 ± 0.0007	$0.0007^{+0.0045}_{-0.0015}$
F	(0.93, 0)	0.6360 ± 0.0072	$0.5378^{+0.0762}_{-0.201}$
G	(1.23, 0)	0.8585 ± 0.0051	$0.8066^{+0.0659}_{-0.1171}$
H	$(\pi, 0)$	0.0004 ± 0.0004	$0.0057^{+0.0123}_{-0.0009}$

Table 2 shows the concurrence of each state before and after distribution. Similar to fidelity, the error of each concurrence was found by conducting Monte-Carlo simulations using the measured counts assuming Poissonian error. At low counts, the concurrence calculated from the density matrix after MLE also did not always match the average concurrence shown by Monte-Carlo simulations. This is also shown in Table 2.

Appendix C: Timing drift

Additionally, long-period measurements were conducted over 52 hours after entanglement distribution over 100-km SMFs to monitor the effect of timing drifts without a feedback system. When measured over 52 hours, we found a total timing drift of each signal and idler counts of approximately 1 ns over 12 hours for each channel depending on the time of day. However, as the lab was well air-conditioned, the fluctuations in timing difference had a standard deviation of 246 ps over 52 hours. We anticipate that extended quantum communication protocols involving multiple entanglement distribution systems or Bell state measurements will require feedback systems to mitigate or get around such timing fluctuations as demonstrated by [10, 53].

Abbreviations

UMZI, unbalanced Mach-Zehnder interferometer; SPDC, spontaneous parametric down conversion; CHSH, Clauser-Horne-Shimony-Holt inequality; DSF, dispersion shifted fiber; SMF, single-mode fiber; DCF, dispersion compensating fiber; CW, continuous wave; SHG, second harmonic generation; IM, intensity modulator; AWG, arbitrary waveform generator; PM, phase modulator; EDFA, erbium-doped fiber amplifier; FBG, fiber Bragg gratings; PPLN, periodically poled lithium niobate; DWDM, dense wavelength-division multiplexer; OSA, optical spectrum analyzer; ITU grid, International Telecommunication Union grid; EPS, entangled photon source; FWHM, full-width half maximum; SNSPD, superconducting nanowire single-photon detector; TCSPC, time-correlated single-photon counting device; CAR, coincidence-to-accidental count ratio; MLE, maximum likelihood estimation.

Acknowledgements

This work is supported by the Institute of Information & Communications Technology Planning & Evaluation (IITP) Grant funded by the Korean government (MSIT) (No. 2022-0-00463, Development of a quantum repeater in optical fiber networks for quantum internet), and by the Electronics and Telecommunications Research Institute (ETRI) grant funded by the Korean government (Grant No. 24ZS1220, Proprietary basic research on computing technology for the disruptive innovation of computational performance).

Author contributions

J.K. and J.P. acquired experimental data, analyzed the data, and wrote the main manuscript text. H.S.K, G.K., J.K, and J.P. acquired experimental data and interpreted experimental data. S.C.K. acquired experimental data. K.M., M.K., and J.J.J. designed and conceived the experiments in the manuscript. All authors reviewed the manuscript.

Funding

This work is supported by the Institute of Information & Communications Technology Planning & Evaluation (IITP) Grant funded by the Korean government (MSIT) (No. 2022-0-00463, Development of a quantum repeater in optical fiber networks for quantum internet), and by the Electronics and Telecommunications Research Institute (ETRI) grant funded by the Korean government (Grant No. 24ZS1220, Proprietary basic research on computing technology for the disruptive innovation of computational performance).

Data availability

The datasets used and analyzed during the current study are available from the corresponding author on reasonable request.

Declarations**Ethics approval and consent to participate**

Not applicable.

Consent for publication

Not applicable.

Competing interests

The authors declare no competing interests.

Author details

¹Quantum Sensing Research Section, Electronics and Telecommunications Research Institute, Daejeon, 34129, Republic of Korea. ²Photonics Planar Integration (PPI), Gwangju, 61008, Republic of Korea.

Received: 8 May 2024 Accepted: 26 August 2024 Published online: 04 September 2024

References

1. Kimble HJ. The quantum internet. *Nature*. 2008;453:1023–30. <https://doi.org/10.1038/nature07127>.
2. Wehner S, Elkouss D, Hanson R. Quantum internet: a vision for the road ahead. *Science*. 2018;362(6412):9288. <https://www.science.org/doi/pdf/10.1126/science.aam9288>. <https://doi.org/10.1126/science.aam9288>.
3. Cacciapuoti AS, Caleffi M, Tafuri F, Cataliotti FS, Gherardini S, Bianchi G. Quantum internet: networking challenges in distributed quantum computing. *IEEE Netw*. 2020;34(1):137–43. <https://doi.org/10.1109/MNET.001.1900092>.
4. Alshowkan M, et al. Reconfigurable quantum local area network over deployed fiber. *PRX Quantum*. 2021;2:040304. <https://doi.org/10.1103/PRXQuantum.2.040304>.
5. Chung J, et al. Illinois Express Quantum Network (IEQNET): metropolitan-scale experimental quantum networking over deployed optical fiber. In: Donkor E, Hayduk M, editors. *Quantum information science, sensing, and computation XIII*. vol. 11726. SPIE; 2021. p. 1172602. <https://doi.org/10.1117/12.2588007>.
6. Briegel H-J, Dür W, Cirac JI, Zoller P. Quantum repeaters: the role of imperfect local operations in quantum communication. *Phys Rev Lett*. 1998;81:5932–5. <https://doi.org/10.1103/PhysRevLett.81.5932>.
7. Ren JG, Xu P, Yong HL, et al. Ground-to-satellite quantum teleportation. *Nature*. 2017;549:70–3.
8. Bouwmeester D, Pan JW, Mattle K, et al. Experimental quantum teleportation. *Nature*. 1997;390:575–9. <https://doi.org/10.1038/37539>.
9. Valivarthi R, Puigibert MG, Zhou Q, Aguilar GH, Verma VB, Marsili F, Shaw MD, Nam SW, Oblak D, Tittel W. Quantum teleportation across a metropolitan fibre network. *Nat Photonics*. 2016;10:676–80.
10. Valivarthi R, et al. Teleportation systems toward a quantum internet. *PRX Quantum*. 2020;1:020317. <https://doi.org/10.1103/PRXQuantum.1.020317>.
11. Bennett CH, Brassard G, Crépeau C, Jozsa R, Peres A, Wootters WK. Teleporting an unknown quantum state via dual classical and Einstein-Podolsky-Rosen channels. *Phys Rev Lett*. 1993;70:1895–9. <https://doi.org/10.1103/PhysRevLett.70.1895>.
12. Zukowski M, Zeilinger A, Horne MA, Ekert AK. “Event-ready-detectors” Bell experiment via entanglement swapping. *Phys Rev Lett*. 1993;71:4287–90. <https://doi.org/10.1103/PhysRevLett.71.4287>.
13. Pan J-W, Bouwmeester D, Weinfurter H, Zeilinger A. Experimental entanglement swapping: entangling photons that never interacted. *Phys Rev Lett*. 1998;80:3891–4. <https://doi.org/10.1103/PhysRevLett.80.3891>.
14. Sun QC, et al. Entanglement swapping over 100 km optical fiber with independent entangled photon-pair sources. *Optica*. 2017;4(10):1214–8. <https://doi.org/10.1364/OPTICA.4.001214>.
15. Neumann SP, Buchner A, Bulla L, et al. Continuous entanglement distribution over a transnational 248 km fiber link. *Nat Commun*. 2022;13:6134. <https://doi.org/10.1038/s41467-022-33919-0>.
16. Wengerowsky S, et al. Entanglement distribution over a 96-km-long submarine optical fiber. *Proc Natl Acad Sci USA*. 2019;116(14):6684–8. <https://doi.org/10.1073/pnas.1818752116>.
17. Wengerowsky S, et al. Passively stable distribution of polarisation entanglement over 192 km of deployed optical fibre. *npj Quantum Inf*. 2020;6:5. <https://doi.org/10.1038/s41534-019-0238-8>.
18. Pelet Y, Sauder G, Cohen M, Labonté L, Alibart O, Martin A, Tanzilli S. Operational entanglement-based quantum key distribution over 50 km of field-deployed optical fibers. *Phys Rev Appl*. 2023;20:044006. <https://doi.org/10.1103/PhysRevApplied.20.044006>.
19. Liu J, Lin Z, Liu D, Feng X, Liu F, Cui K, Huang Y, Zhang W. High-dimensional quantum key distribution using energy-time entanglement over 242 km partially deployed fiber. *Quantum Sci Technol*. 2024;9:015003. <https://doi.org/10.1088/2058-9565/acfe37>.
20. Fitzke E, Bialowons L, Dolejsky T, Tippmann M, Nikiforov O, Walther T, Wessel F, Gunkel M. Scalable network for simultaneous pairwise quantum key distribution via entanglement-based time-bin coding. *PRX Quantum*. 2022;3:020341. <https://doi.org/10.1103/PRXQuantum.3.020341>.
21. Brendel J, Gisin N, Tittel W, Zbinden H. Pulsed energy-time entangled twin-photon source for quantum communication. *Phys Rev Lett*. 1999;82:2594–7. <https://doi.org/10.1103/PhysRevLett.82.2594>.
22. Inagaki T, Matsuda N, Tadanaga O, Asobe M, Takesue H. Entanglement distribution over 300 km of fiber. *Opt Express*. 2013;21(20):23241–9. <https://doi.org/10.1364/OE.21.023241>.
23. Honjo T, et al. Long-distance entanglement-based quantum key distribution over optical fiber. *Opt Express*. 2008;16(23):19118–26. <https://doi.org/10.1364/OE.16.019118>.

24. Li D-D, et al. Field implementation of long-distance quantum key distribution over aerial fiber with fast polarization feedback. *Opt Express*. 2018;26(18):22793–800. <https://doi.org/10.1364/OE.26.022793>.
25. Fitzke E, Bialowons L, Dolejsky T, Tippmann M, Nikiforov O, Walther T, Wissel F, Gunkel M. Scalable network for simultaneous pairwise quantum key distribution via entanglement-based time-bin coding. *PRX Quantum*. 2022;3:020341. <https://doi.org/10.1103/PRXQuantum.3.020341>.
26. Hübner H, Vanner MR, Lederer T, Blauensteiner B, Lorünser T, Poppe A, Zeilinger A. High-fidelity transmission of polarization encoded qubits from an entangled source over 100 km of fiber. *Opt Express*. 2007;15(12):7853–62. <https://doi.org/10.1364/OE.15.007853>.
27. Wei T-C, Altepeter JB, Branning D, Goldbart PM, James DFV, Jeffrey E, Kwiat PG, Mukhopadhyay S, Peters NA. Synthesizing arbitrary two-photon polarization mixed states. *Phys Rev A*. 2005;71:032329. <https://doi.org/10.1103/PhysRevA.71.032329>.
28. Bussi eres F, Slater JA, Jin J, Godbout N, Tittel W. Testing nonlocality over 12.4 km of underground fiber with universal time-bin qubit analyzers. *Phys Rev A*. 2010;81:052106. <https://doi.org/10.1103/PhysRevA.81.052106>.
29. Kupchak C, Bustard PJ, Heshami K, Erskine J, Spanner M, England DG, Sussman BJ. Time-bin-to-polarization conversion of ultrafast photonic qubits. *Phys Rev A*. 2017;96:053812. <https://doi.org/10.1103/PhysRevA.96.053812>.
30. Valiwarthi R, et al. Efficient bell state analyzer for time-bin qubits with fast-recovery WSi superconducting single photon detectors. *Opt Express*. 2014;22(20):24497–506. <https://doi.org/10.1364/OE.22.024497>.
31. Cabrejo-Ponce M, Spiess C, Muniz ALM, Ancsin P, Steinlechner F. Ghz-pulsed source of entangled photons for reconfigurable quantum networks. *Quantum Sci Technol*. 2022;7(4):045022. <https://doi.org/10.1088/2058-9565/ac86f0>.
32. Grice WP, Beck M, Earl D, Mulkey D, Schaake J. Reconfigurable entangled photon source (conference presentation). In: Gruneisen MT, Dusek M, Alsing PM, Rarity JG, editors. *Quantum technologies and quantum information science V*. vol. 11167. SPIE; 2019. p. 111670. <https://doi.org/10.1117/12.2536266>.
33. Williams BP, Lukens JM, Peters NA, Qi B, Grice WP. Quantum secret sharing with polarization-entangled photon pairs. *Phys Rev A*. 2019;99:062311. <https://doi.org/10.1103/PhysRevA.99.062311>.
34. Agrawal P, Pati AK. Probabilistic quantum teleportation. *Phys Lett A*. 2002;305(1):12–7. [https://doi.org/10.1016/S0375-9601\(02\)01383-X](https://doi.org/10.1016/S0375-9601(02)01383-X).
35. Modl awska J, Grudka A. Nonmaximally entangled states can be better for multiple linear optical teleportation. *Phys Rev Lett*. 2008;100:110503. <https://doi.org/10.1103/PhysRevLett.100.110503>.
36. Marcikic I, Riedmatten H, Tittel W, Scarani V, Zbinden H, Gisin N. Time-bin entangled qubits for quantum communication created by femtosecond pulses. *Phys Rev A*. 2002;66:062308. <https://doi.org/10.1103/PhysRevA.66.062308>.
37. Takesue H, Noguchi Y. Implementation of quantum state tomography for time-bin entangled photon pairs. *Opt Express*. 2009;17(13):10976–89. <https://doi.org/10.1364/OE.17.010976>.
38. Clauser JF, Horne MA, Shimony A, Holt RA. Proposed experiment to test local hidden-variable theories. *Phys Rev Lett*. 1969;23:880–4. <https://doi.org/10.1103/PhysRevLett.23.880>.
39. Kim J-H, Chae J-W, Jeong Y-C, Kim Y-H. Long-range distribution of high-quality time-bin entangled photons for quantum communication. *J Korean Phys Soc*. 2022;80:203–13. <https://doi.org/10.1007/s40042-021-00342-5>.
40. Zhao J, Ma C, R using M, Mookherjee S. High quality entangled photon pair generation in periodically poled thin-film lithium niobate waveguides. *Phys Rev Lett*. 2020;124:163603. <https://doi.org/10.1103/PhysRevLett.124.163603>.
41. Sedziak-Kacprowicz K, Czerwinski A, Kolenderski P. Tomography of time-bin quantum states using time-resolved detection. *Phys Rev A*. 2020;102:052420. <https://doi.org/10.1103/PhysRevA.102.052420>.
42. Fasel S, Gisin N, Ribordy G, Zbinden H. Quantum key distribution over 30 km of standard fiber using energy-time entangled photon pairs: a comparison of two chromatic dispersion reduction methods. *Eur Phys J D*. 2004;30:143–8. <https://doi.org/10.1140/epjd/e2004-00080-8>.
43. Joshi SK, et al. A trusted node-free eight-user metropolitan quantum communication network. *Sci Adv*. 2020;6(36):0959. <https://www.science.org/doi/pdf/10.1126/sciadv.aba0959>. <https://doi.org/10.1126/sciadv.aba0959>.
44. Wengerowsky S, Joshi SK, Steinlechner F, Hubel H, Ursin R. An entanglement-based wavelength-multiplexed quantum communication network. *Nature*. 2018;564:225–8.
45. Marcikic I, Riedmatten H, Tittel W, Zbinden H, Legr e M, Gisin N. Distribution of time-bin entangled qubits over 50 km of optical fiber. *Phys Rev Lett*. 2004;93:180502. <https://doi.org/10.1103/PhysRevLett.93.180502>.
46. Zhong T, Wong FNC, Restelli A, Bienfang JC. Efficient single-spatial-mode periodically-poled ktiopo4 waveguide source for high-dimensional entanglement-based quantum key distribution. *Opt Express*. 2012;20(24):26868–77. <https://doi.org/10.1364/OE.20.026868>.
47. Zhong T, Wong FNC. Nonlocal cancellation of dispersion in franson interferometry. *Phys Rev A*. 2013;88:020103. <https://doi.org/10.1103/PhysRevA.88.020103>.
48. Dynes JF, et al. Efficient entanglement distribution over 200 kilometers. *Opt Express*. 2009;17(14):11440–9. <https://doi.org/10.1364/OE.17.011440>.
49. Aspect A, Dalibard J, Roger G. Experimental test of Bell's inequalities using time-varying analyzers. *Phys Rev Lett*. 1982;49:1804–7. <https://doi.org/10.1103/PhysRevLett.49.1804>.
50. Altepeter JB, Jeffrey ER, Kwiat PG. Photonic state tomography. In: *Advances in atomic, molecular, and optical physics*. vol. 52. San Diego: Academic Press; 2005. p. 105–59. <https://www.sciencedirect.com/science/article/pii/S1049250X05520032>. [https://doi.org/10.1016/S1049-250X\(05\)52003-2](https://doi.org/10.1016/S1049-250X(05)52003-2).
51. James DFV, Kwiat PG, Munro WJ, White AG. Measurement of qubits. *Phys Rev A*. 2001;64:052312. <https://doi.org/10.1103/PhysRevA.64.052312>.
52. Banaszek K, D'Ariano GM, Paris MGA, Sacchi MF. Maximum-likelihood estimation of the density matrix. *Phys Rev A*. 1999;61:010304. <https://doi.org/10.1103/PhysRevA.61.010304>.
53. Shen S, Yuan C, Zhang Z, et al. Hertz-rate metropolitan quantum teleportation. *Light: Sci Appl*. 2023;12:115. <https://doi.org/10.1038/s41377-023-01158-7>.

Publisher's Note

Springer Nature remains neutral with regard to jurisdictional claims in published maps and institutional affiliations.